Atomistic study on the anomalous temperature-dependent dynamic tensile strength of ice under shock loading

Y. Y. Chen, K. L. Xiao, J. Z. Yue, Q. Y. Yin, X. Q. Wu & C. G. Huang

Taylor & Francis
Taylor & Francis Group

Check for updates

Atomistic study on the anomalous temperature-dependent dynamic tensile strength of ice under shock loading

Y. Y. Chen[a,b], K. L. Xiao[a,b], J. Z. Yue[a], Q. Y. Yin[c,f], X. Q. Wu[a,e] and C. G. Huang[a,d]

[a]Institute of Mechanics, Chinese Academy of Sciences, Beijing, People's Republic of China; [b]School of Engineering Science, University of Chinese Academy of Sciences, Beijing, People's Republic of China; [c]Department of Applied Mechanics & Engineering, School of Engineering, Sun Yat-sen University, Guangzhou, People's Republic of China; [d]Hefei Institutes of Physical Science, Chinese Academy of Sciences, Hefei, People's Republic of China; [e]Materials and Process Simulation Center, California Institute of Technology, Pasadena, CA, USA; [f]School of Aerospace Engineering, Xi'an Jiaotong University, Xi'an, People's Republic of China

ABSTRACT

Although the compressive strength of ice under both quasi-static [M. Arakawa and N. Maeno, Mechanical strength of polycrystalline ice under uniaxial compression. Cold Reg. Sci. Tech 26 (1997), pp. 215–229.] and dynamic [X. Wu and V. Prakash, Dynamic compressive behavior of ice at cryogenic temperatures. Cold Reg. Sci. Tech 118 (2015), pp. 1–13.] loadings shows an anomalous temperature effect that the compression strength is insensitive to temperature in a specific temperature range below −100°C, it is still unclear whether the anomalous temperature exists for the tensile strength of ice at cryogenic temperatures. In this paper, the temperature-dependent dynamic tensile strength of ice 1 h under shock loading is investigated by molecular dynamics simulations. It is intriguing to see that the dynamic tensile strength of the ice exhibits a similar anomalous temperature effect, i.e. it is almost insensitive to temperature in the range 117 ∼ 163 K, which could be interpreted by the competitive mechanism between shock-induced pulverisation and melting. The evolution of the pentagonal-heptagonal defects and the ductile-to-brittle transformation are also observed with decreasing temperature, leading to the unique dynamic tensile behaviour of ice under shock.

1. Introduction

Ice constitutes the second most massive solid after the lithosphere globally and plays an essential role in the water cycle. The dynamic behaviour of ice under

CONTACT Q.Y. Yin ✉ yinqy5@mail.sysu.edu.cn Department of Applied Mechanics & Engineering, School of Engineering, Sun Yat-sen University, Guangzhou 510275, People's Republic of China; School of Aerospace Engineering, Xi'an Jiaotong University, Xi'an 710049, People's Republic of China; X.Q. Wu ✉ wuxianqian@imech.ac.cn Institute of Mechanics, Chinese Academy of Sciences, Beijing 100190, People's Republic of China; Materials and Process Simulation Center, California Institute of Technology, Pasadena, CA 91125, USA

high strain-rate loading is an essential issue in glaciology, geophysics, and polar engineering. For example, the accelerated flow of fractured glaciers resulting from the collapse of the Larsen B ice shelf, drifting in response to tides [1], significantly affected the polar landforms and ecosystems and became a hotspot of global warming [2]. A better understanding of the dynamic properties of ice is beneficial for disaster evaluation and mitigation of the collapse event. Besides the earth, ice is also widely distributed in the solar system [3], urging the research on the dynamic behaviour for extraterrestrial life detection and exploration of some icy moons.

The mechanical behaviour of ice is complicated due to various crystal structures at different temperatures and pressures [4]. There is a large body of literature that addresses the mechanical behaviour of ice at various loading rates and temperatures. Currier [5] reported that the tensile strength of ice decreases with increasing grain size but exhibits insensitivity to the strain rate at $-10°C$ because cracks at the grain interface can readily propagate. In contrast, the compressive strength of the ice, reported by Schulson et al. [6,7], is sensitive to the deformation rate and temperature. At $-10°C$, a ductile-to-brittle transformation of ice with a grain size of ~1 mm is observed as the strain rate increased from 10^{-8} to 10^{-3} s^{-1}, and the compressive strength dramatically increases from 0.5 to 10 MPa. In the temperature range from -10 to $-50°C$, the brittle fractures are generally occurred at the constrained end of the ice specimen with the predominant failure mode of shear fracture and, to a lesser extent, axial splitting. Once decreasing the test temperature to about $-100°C$, an anomalous experimental phenomenon is observed that the effects of temperature can be neglected. Arakawa [8] studied the uniaxial compression strength of ice 1 h at a strain rate of 4×10^{-5} s^{-1} and temperatures ranging from -10 to $-173°C$. The results showed that two distinct brittleness regions exist at a critical point of $-103°C$, and the compression strength is not sensitive to temperatures below $-103°C$. Based on Arakawa's experimental data [8], it was noted that there is a plateau for the maximum stress in the temperature range $-103 \sim -130°C$. A similar phenomenon was observed in dynamic compression experiments. The study by Wu and Prakash [9] illustrated that the dynamic compressive strength of the ice is maintained at about 115 MPa with temperatures ranging from -125 to $-150°C$, and strain rates ranging from 220 to 500 s^{-1} through a modified split Hopkinson pressure bar (SHPB) experiment. However, the ice's strength increases again but does not show noticeable strain rate sensitivity when continually decreasing the temperature to $-175°C$. One thing should be pointed out that the ice samples in Wu and Prakash [9] experiments were highly fragmented as dry granular powders below $-125°C$, while compressed into new-cluster as fine-grained wet granular materials above $-80°C$.

According to the literature available, the compressive strength of ice generally increases with decreasing test temperatures. However, there is an

anomalous temperature range for ice, in which the compressive strength of ice is insensitive to temperature as observed by Arakawa [8] in the temperature range −103 ∼ −130°C under quasi-static loading and Wu and Prakash [9] in the temperature range −125 ∼ −150°C under high strain rate loading. Wu and Prakash [9] supposed that the anomalous temperature effects might result from the ice phase transformation during dynamic compression. Recently, Yin *et al.* [10] performed uniaxial uniform compression of ice at high strain rates through molecular dynamics (MD) simulations, and a stable solid–solid phase transition of single-crystal ice at 163 K was observed, which is consistent with the speculation of Wu and Prakash [9]. However, these studies did not consider tensile loading conditions, which is vital to better understand the high-speed icebreaking behaviour in polar exploration and crater formation of icy moons of some planets in outer space. Therefore, an intriguing question arises: does the anomalous temperature effect still exist for the tensile strength of ice under dynamic loading? Up to now, no experimental or numerical simulation evidence has been reported to answer this question to the best knowledge of the authors.

In this paper, the effect of temperature on the dynamic tensile strength of ice 1 h is investigated by MD simulations. Similar as the anomalous temperature effect on the compressive strength of ice, an anomalous temperature effect on the dynamic tensile strength of the ice is observed for the first time, which contributes to the understanding of ice science under high strain rates. Moreover, the corresponding mechanism is analysed from the deformation mode of the ice at different temperatures. The paper is organised as follows. Section 2 details the MD simulation model of ice 1 h under dynamic loading. Section 3 presents the stress wave attenuation and the anomalous temperature-dependent dynamic tensile strength of ice. The deformation and failure behaviour of the ice under shock loading are also investigated to explain the temperature effects, followed by discussions and conclusions.

2. Methods

The SPC/E model, which is developed by Berendsen [11] and has been widely used for efficiently handling bulk water simulations [12–14], is adopted in the simulations. Figure 1 shows the unit of the ice 1 h (*i.e.* contains five molecules and forms an open tetrahedral crystal cell) based on the parameters of the SPC/E model, where a single water molecule consists of one oxygen atom (red sphere) and two hydrogen atoms (white sphere). The bond length between the hydrogen atom and oxygen atom is 1 Å at the equilibrium state, the interatomic angle of hydrogen–oxygen-hydrogen atoms is 109.47°, and the angle between each water molecule and the four adjacent ones is 104.52°. Each water molecule has two lone-pair electrons and two covalent bonds corresponding to the sp3 hybridisation type. One lone-pair electron can form a
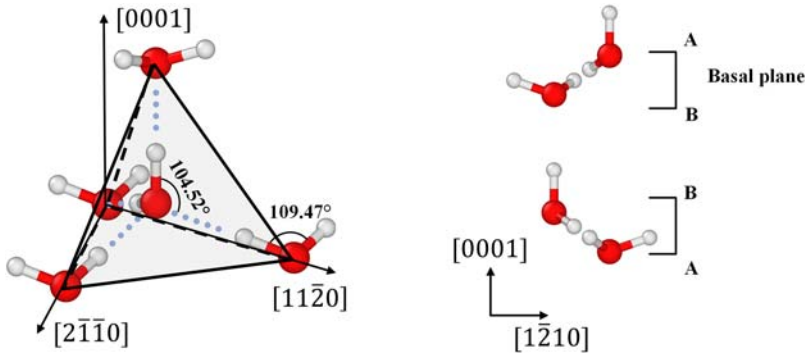
Figure 1. A unit cell of ice1 h constructed with the SPC/E parameters.

hydrogen bond with a hydrogen atom on another water molecule (*i.e.* each water molecule participates in four hydrogen bonds). The molecular layers distributed in parallel along the [0 0 0 1] direction are defined as basal planes, and the sequence of the basal planes stacking is … ABBA ABBA … , leading to a packing factor of only 0.36 for ice 1 h. Its sparse arrangement of molecules can explain many physical properties of ice, such as its lower density than water and its melting point decreasing at a rate of 0.074 °C/MPa under high pressure [15].

Figure 2 shows the schematic of the simulation model. A column body with dimensions of 40.689 × 469.92 × 44.172 Å is constructed by extending the ice 1 h crystal cell along the [1 0 $\bar{1}$ 0], [$\bar{1}$ 2 $\bar{1}$ 0], and [0 0 0 1] directions, respectively. Since the dislocations are more likely to occur between the basal planes, the [$\bar{1}$ 2 $\bar{1}$ 0] direction (*i.e.* zigzag direction) is set as the impact loading direction. Atoms in the range of 16 Å from the impact end are selected as a rigid piston to provide a given initial impact velocity of 950 m/s. Vacant spaces are reserved at both ends along the impact direction in response to the structural deformation, and the periodic boundary conditions are applied on the rest facets perpendicular to the impact direction.

The simulations are performed by the large-scale atomic/molecular massively parallel simulator (LAMMPS) [16], and the intermolecular forces are
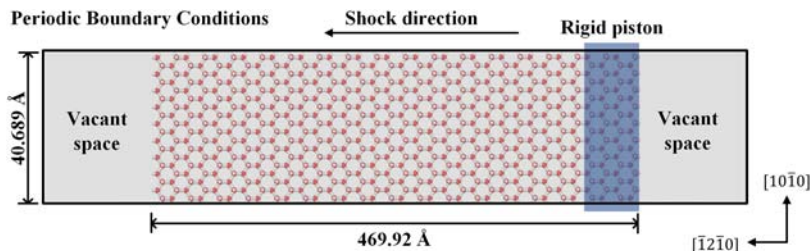

Figure 2. Schematic of the MD model subjected to impact loading.

described by the Lennard-Jones (LJ) potential functions and Coulomb interactions,

$$LJ(r) = 4\varepsilon\left[\left(\frac{\sigma}{r}\right)^{12} - \left(\frac{\sigma}{r}\right)^{6}\right], \tag{1}$$

$$C(r) = \frac{Cq_iq_j}{\varepsilon r}, \tag{2}$$

where ε is the depth of the potential well, and σ denotes the distance between atoms when the potential energy is equal to zero. The ε and σ are set to be 0.1553 kcal/mol and 3.166 Å, respectively, between oxygen and oxygen atoms, and are set to be 0 kcal/mol and 2.058 Å, respectively, between hydrogen and hydrogen atoms. The force between hydrogen and oxygen atoms is determined by the Lorentz-Berthelot mixing rules [17].

During the initial thermo-relaxing, the temperature and pressure of the system are controlled by the Nose–Hoover method [18]. The initial temperature is kept at 263 K, and the initial pressure is controlled at 1 atmosphere (atm). After relaxation, the system is cooled down to the target temperature and relaxed again. The timestep is 1 femtosecond (fs), and the entire process is performed for 750 picoseconds (ps) to ensure the total energy fluctuation is less than 0.1%. After the system arrives at the equilibrium state, the subsequent loading process is conducted in the NVE ensemble. The rigid piston is given a uniform impact velocity of 950 m/s with a duration of 3 ps. Then, the dynamic responses of the system are observed in the next 60 ps.

3. Results and discussion

3.1. Stress wave attenuation

The typical stress and temperature time-position nephograms at the relaxation temperature of 163 K and the impact velocity of 950 m/s are depicted in Figure 3 to visualise the thermodynamic properties and stress wave propagation behaviour of the ice. The position information in the nephogram is given by the Lagrangian coordinates fixed on the rigid piston, and the area occupied by the atoms representing the vacant space is shown as null values (depicted by grey areas). As shown in Figure 3(a), the compressive stress wave with an amplitude of about 4 GPa is initially generated once the piston impacts the ice. The compressive stress wave attenuates during propagation and arrives at the back free surface at about 15 ps. Therefore, the sound wave speed of the ice is estimated to be 3.13 km/s, which is consistent with the study by Wu and Prakash [9]. Then the compressive stress wave reflects at the back free surface, and the tensile stress wave is formed and propagates towards the impact end. If the tensile stress exceeds the dynamic tensile strength of the ice, the spalling of ice occurs, and
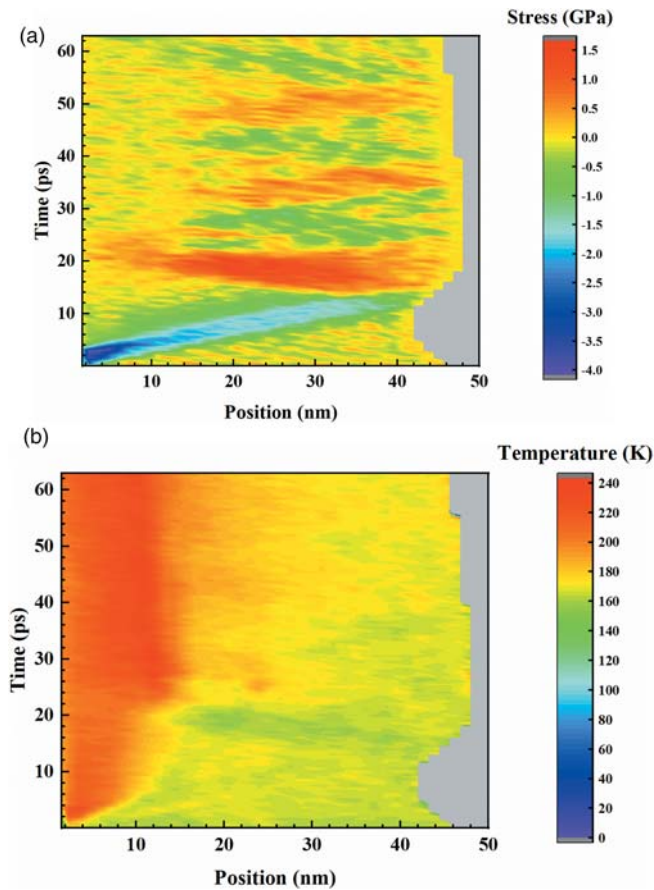
Figure 3. (a) Stress wave propagation and (b) structural temperature rising at a relaxation temperature of 163 K and impact velocity of 950 m/s.

consequently, the dynamic tensile strength of the ice can be determined. As shown in Figure 3(b), with the propagation of the stress waves, the temperature of the region near the impact end increases quickly, and the high-temperature region expands slowly in the following loading process of the stress waves. Since the stresses and temperatures are calculated by accumulating the information on all the atoms within the micro-element, it is difficult to discern the characteristics of the fracture behaviour of the ice in the stress and temperature time-position nephograms.

Figure 4 shows the stress histories at various positions away from the impact end and the stress distributions along the length of the ice specimen at various instants, where the shaded fills of the curves indicate statistical errors. As shown in Figure 4(a), during propagation, the peak stress of the first compressive wave attenuates almost exponentially from 3.2 GPa at 9.2 to 1.8 GPa at 38.5 nm. Of particular note is that there is an anomalous peak stress enhancement (at about 25 ps) at 28.6 nm compared to that at 19.1 nm during the second compressive
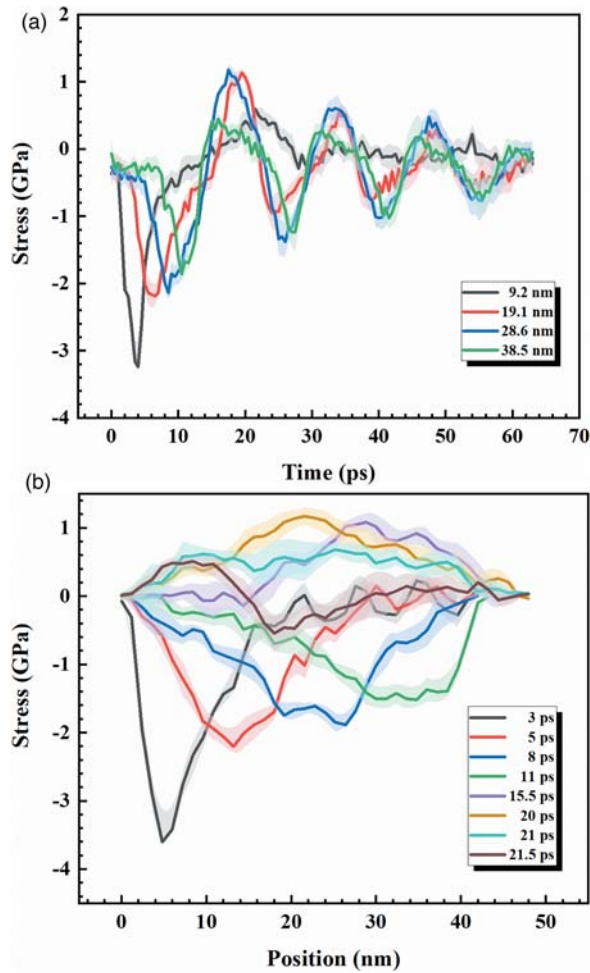
Figure 4. Stress wave attenuation at a relaxation temperature of 163 K and impact velocity 950 m/s. (a) Stress histories at different locations far from the impact end of the model. (b) Stress distributions along the impact direction at different instants.

wave propagation. We speculate that there might be a fractured layer resulted from the first tensile stress wave between 19.1 and 28.6 nm. When the second compressive propagates through the 19.1 nm position, it will partially reflect at the free boundary of the fracture surface. With continuous loading, the fracture could re-bond, leading to a relatively higher compressive peak stress at 28.6 than that at 19.1 nm. Similar processes are observed during the propagation of the subsequent compressive stress waves. As shown in Figure 4(b), we can also clearly see the attenuation of the stress wave. In addition, the first compression wave is gradually flattened during the propagation from 3 to 11 ps due to the dissipation of atoms vibration and defects formation. Moreover, it is seen that the profile of the tensile stress wave at 21 ps collapses at about 20 nm far from the impact end into the two-section profile at 21.5 ps, indicating

the occurrence of tensile stress-induced fracture at about 20 nm, which is consistent with the observation in Figure 4(a).

3.2. Temperature-dependent dynamic tensile strength

Based on the stress wave analysis, the dynamic tensile strengths of the ice at various cryogenic temperatures ranging from 73 to 215 K are obtained, as given in Figure 5. The data with different symbols and colours correspond to different tensile-induced fracture modes, which will be explained in detail in the following sections. For each point, multiple simulations are performed to get the average value and error. It is intriguing to note that the dynamic tensile strength of the ice also shows anomalous temperature effects similar to those observed by the Arakawa [8] and Wu and Prakash [9] in compression experiments. The temperature effects on the dynamic tensile strength of the ice can be divided into four regions, as follows:

- With decreasing temperature from 215 to 163 K, the dynamic tensile strength of the ice increases from 1.21 to 1.56 GPa, showing noticeable temperature sensitivity.
- The dynamic tensile strength maintains at about 1.5 GPa in the temperature range 117 ~163 K, showing nearly temperature independence.
- The dynamic tensile strength continually increases to 2.04 GPa by decreasing the temperature to 100 K.
- The dynamic tensile strength decreases again to 1.86 GPa by decreasing the temperature to 73 K.

The anomalous dynamic tensile strengths of ice at various temperatures should be ascribed to the dynamic deformation and failure behaviour of the
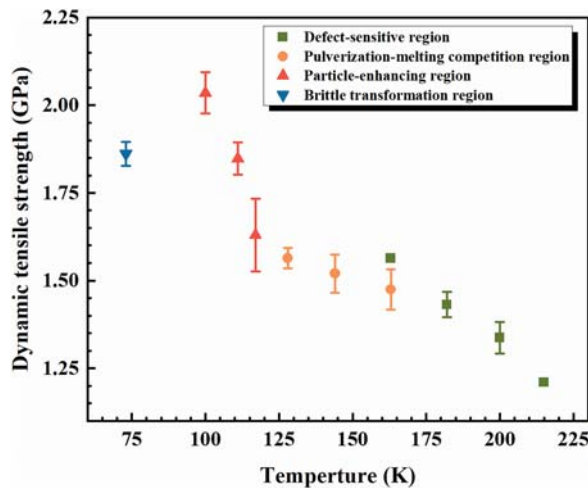

Figure 5. The temperature effect on the dynamic tensile strength in ice 1 h.

ice under both compressive and tensile stress waves, which will be investigated in the next sections.

3.3. Phase transformation and crystal defect evolution under compression

The microstructure evolution under compressive is essential to understand the complex temperature effects of the dynamic tensile strength of the ice. As shown in Figure 6(a), during loading, the oxygen atoms in the system can be divided into four categories according to their relative spatial positions deviating from the hexagonal crystalline lattice: the red oxygen atoms that their first and second nearest neighbours are in the hexagonal diamond lattice (denoted as 'hexagonal diamond'); the yellow oxygen atoms that only the four first nearest neighbour atoms are in the correct lattice position (denoted as 'hexagonal diamond 1st neighbor'); the green oxygen atoms that are the second nearest neighbour of the red oxygen atom, and all of their first nearest neighbour atoms deviate from the correct lattice position (denoted as 'hexagonal diamond 2nd neighbor'); the grey oxygen atoms that do not belong to any of the classes mentioned above (denoted as 'other'). With the propagation of the compressive stress wave, the hexagonal structures are compressed at the front of the wave, leading to the solid–solid phase transition as the observation of Yin et al. [10] and the formation of the pentagonal-heptagonal defects as depicted in detail in Figure 6(b), where the two adjacent layers of water molecules stacked in different ways are distinguished in red and blue (also known as the glide set [15]), and the hydrogen atoms are hidden to show the evolution
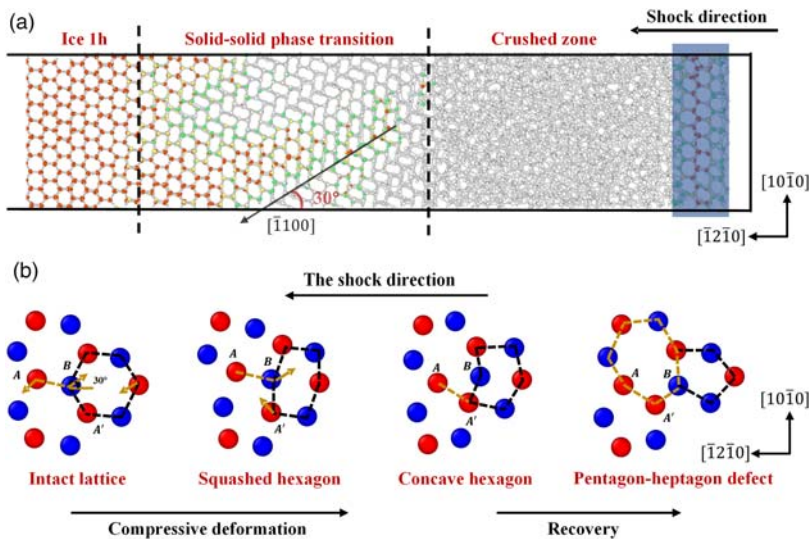

Figure 6. The microstructural evolution of ice1 h under shock loading. (a) Compression-induced phase transition, pentagonal-heptagonal defects, and crushed failure of the ice. (b) Schematic of the evolution of compression-induced pentagonal-heptagonal defects.

process clearly. Here, the atom A and atom A' denote the first nearest neighbours of the atom B as shown in Figure 6(b). Initially, all the oxygen atoms are at the thermal-equilibrium positions of the hexagonal diamond lattice. Under compression, the two regularly arranged adjacent layers of water molecular undergo shear deformation in the direction of maximum shear stress (*i.e.* the [$\bar{1}$100] direction), where the atom A and atom A' get closer and flatten the lattice, forming a new phase with a lower symmetry (transformed into a monoclinic cell). The atom B detaches from the initial position with further compression, and the lattice (indicated by the black dashed line) transforms into a concave hexagonal structure. During unloading, the detachment of the atom B weakens the force between the atoms A and B while shortening the distance between the atoms A and A', leading to the bond breaking between the atoms A and B and the bond formation between the atoms A and A'. As a result, the pentagonal-heptagonal defect is left. The solid–solid phase boundary propagates along [$\bar{1}$100] under the compressive stress wave, followed by a crushed zone near the impact end.

The degree of the structural damages caused by the compression wave, including the pentagonal-heptagonal defects, the melting, and the pulverisation of the crushed zone, could influence the locations of subsequent fractures and the dynamic tensile strengths of the ice at various temperatures. Therefore, the proportions of the four types of oxygen atoms at 15 ps when the compression wave propagates to the back surface are calculated as shown in Figure 7(a) to investigate the structural damage. Here, the content of the red oxygen atoms indicates the intact lattice, the content of the gray oxygen atoms mainly reflects the complete melting, and the content of yellow and green oxygen atoms represents the pentagonal-heptagonal defects or the incomplete melting in the crushed zone. It can be seen that as the temperature decreases, the melting content decreases, and the intact lattices increase. With decreasing the temperature from 215 to 163 K, the proportion of the green and the yellow oxygen atoms decreases from 20 to 13%. Then it maintains at about 6% in the temperature range 117 ~ 163 K, indicating a significant decrease in the number of lattice defects in the ice. As the temperature decreases from 117 K to 73 K, the content of the grey oxygen atoms decreases from 18% to 13%, while the content of the yellow and the green oxygen increases from 6.4% to 8.5%.

Figure 7(b) shows the schematics of the structural damage after compression at various temperatures and the ratio between the content of yellow and green oxygen atoms and the content of gray oxygen atoms, i.e. the damage-to-melt ratio. In the temperature range 182 ~ 215 K, the damage-to-melt ratio is maintained at about 55%, corresponding to the stacked crystal defects and the compression-induced local melting observed in the model. When the temperature drops to 163 K, the damage-to-melt ratio rapidly decreased to 32%, accompanied by a significant reduction in the number of defects. In addition, the damage-to-melt ratio keeps at almost the same level of 28% at various
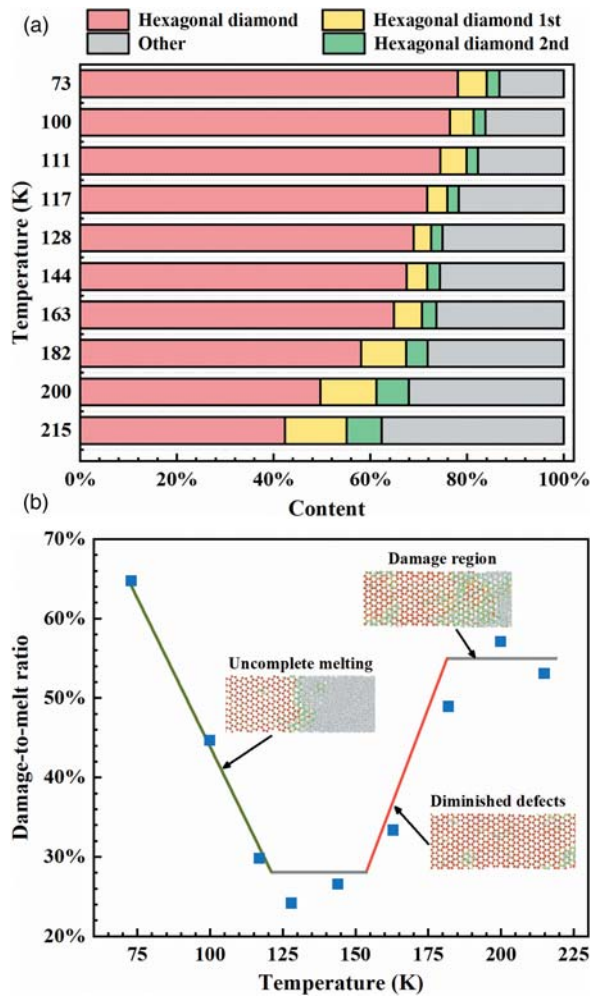
Figure 7. (a) The proportions of the four types of oxygen atoms and (b) the damage-to-melt ratio of the ice under compression at various temperatures ranging from 73 to 215 K.

temperatures from 117 to 163 K, indicating that the melting (or pulverisation) in the crushed zone is approximately at the same degree. As the temperature decreases from 117 to 73 K, the damage-to-melt ratio is gradually increased to 64%. It is noteworthy that no obvious defects are observed in the ice in this temperature range, suggesting that the enhancement of the damage-to-melt ratio is mainly attributed by the incomplete melting in the crushed zone.

3.4. Tension-induced failure modes of the ice

When the compressive wave reflects at the back free surface, the tensile wave is generated and propagates in the ice, leading to the fracture of the ice at a compressive-induced damage region. The anomalous temperature effects of the

dynamic tensile strength of the ice, as given in Figure 5, could be explained by temperature-dependent fracture modes under dynamic tension loadings. At a relatively high-temperature above 163 K (corresponding to the green data in Figure 5), the compression-induced pentagonal-heptagonal defects deform under dynamic tension, as shown in Figure 8(a). The bonds of the heptagonal structure begin to break, resulting in the micro-cracks perpendicular to the loading direction and eventual fracture of this section. As shown in Figure 8 (b) (the blue surface represents the fracture morphology obtained by the alpha-shape algorithm [19, 20]), no obvious melt is observed in the tension-induced fracture region, and the fracture morphology shows somewhat micro-plasticity as evidence by the fibrous characteristics. As the temperature decreases for the temperature higher than 163 K, the degree of local melting and the number of defects decreases, resulting in an increase of the dynamic tensile strength of the damage region.

As the temperature drops below 163 K, the location of the tension-induced fracture shifts from the compression-induced pentagonal-heptagonal defects to the crushed zone due to the increase of the strength of the local damaged region. Although the failure locations and the fracture morphologies are similar, the deformation mechanisms of the ice in the temperature range 163 ~ 100 K could be divided into two sections. One is the pulverisation-melting competition in the temperature range 117 ~ 163 K, as given by the orange data in Figure 5, where the strengthening mechanism of pulverised grains competes with the weakening mechanism of melting, resulting in the temperature insensitivity of the tensile strength. The second is the particle-enhancement in the temperature range 100 ~ 117 K as depicted by the red data in Figure 5, in which the melting degree of the crushed region near the impact end reduces significantly,
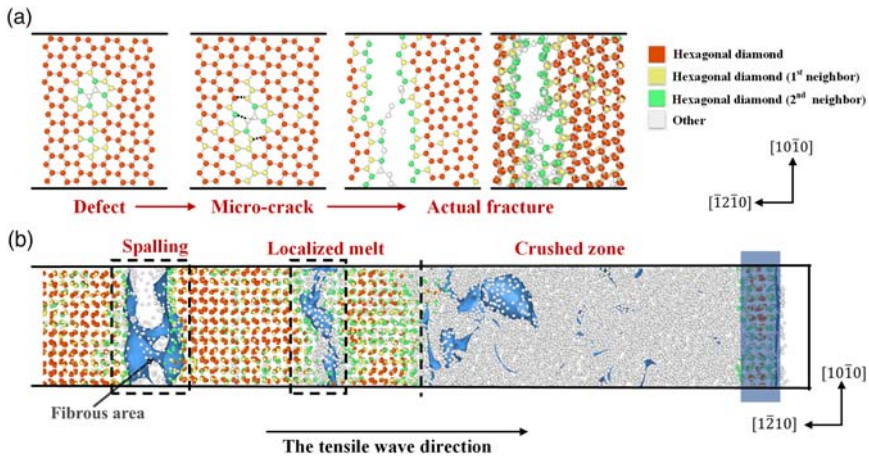

Figure 8. Fracture modes of ice 1 h at relaxation temperatures above 163 K. (a) Fracture morphology of the damage region. (b) Schematic representation of tensile wave-induced crack propagation.

and the deformation of the fracture region is dominated by the particle refinement of the ice with decreasing temperature, leading to the appearance of temperature effect of the dynamic tensile strength of the ice in this temperature region.

Figure 9(a) shows the radial distribution functions (RDFs) at various temperatures in the range 73 ~ 200 K. The curves represent the spatial distribution of a 4-nm-thick oxygen atom layer in the crushed zone after compression, where the extreme point and the full width at half maximum (FWHM) of the RDFs' first peak indicate the relative distance and the average displacement between two neighbour oxygen atoms of a stable ice-1 h lattice, respectively. As a comparison, the RDF of an equivalent-sized SPC/E ice model relaxed for 750 ps at 100 K, and 1 atm is also calculated as a reference, as shown in Figure 9(a). The normalised FWHMs at various temperatures based on the reference value are given in Figure 9(b). As shown in Figure 9(a), in the
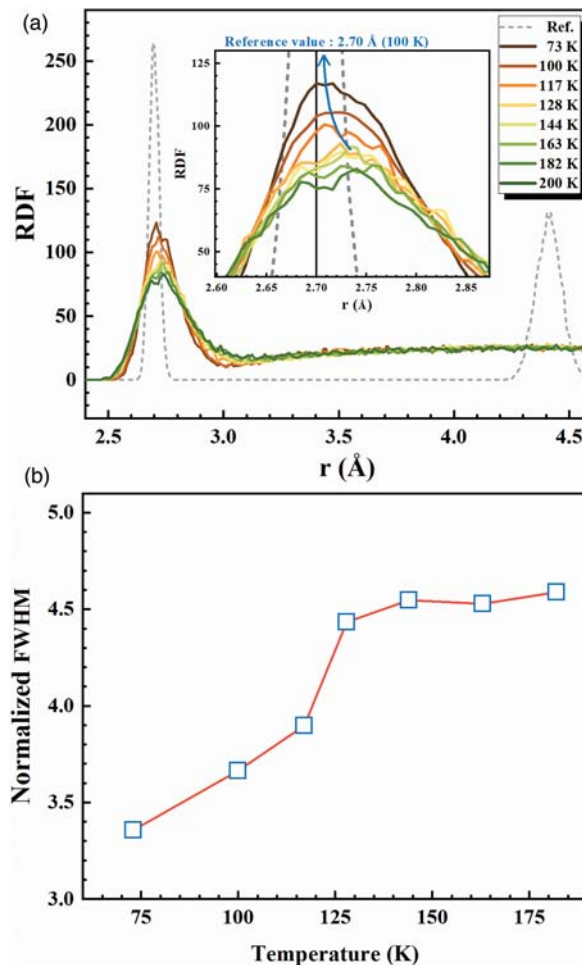

Figure 9. (a) Radial distribution functions (RDFs) of the crushed zone and (b) the normalised FWHM at temperatures from 73 to 200 K.
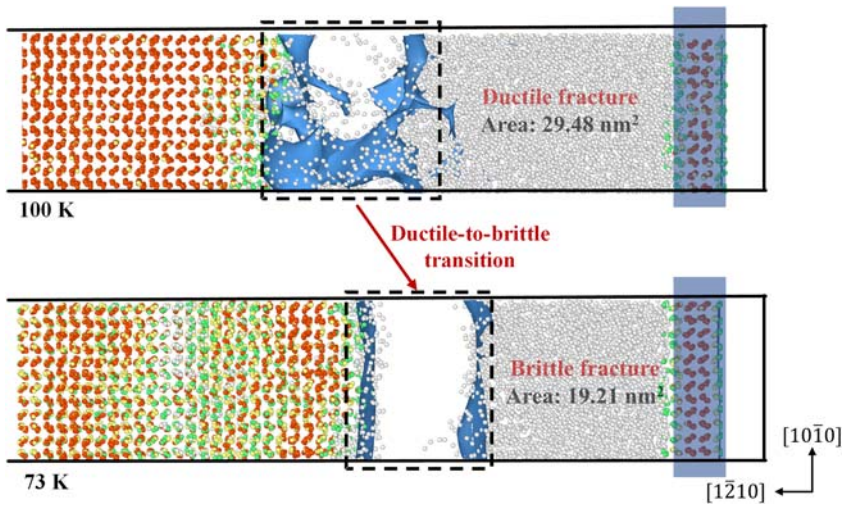
Figure 10. Fracture morphologies of the ice at 100 and 73 K, indicating the ductile-to-brittle fracture transition.

temperature range 163~117 K, i.e. the pulverisation-melting competition region in Figure 5, the extreme point change with respect to temperature is insignificant. As the temperature decreases below 117 K (i.e. the particle-enhancing region in Figure 5), the extreme point rapidly approaches the reference value and remains below 2.71 Å. These results indicate that below 117 K, the short-range orderings of the nearest neighbour atomic structures in the crushed zone begin to enhance significantly with decreasing temperature, leading to the increase of the tensile strength with particle refinement. The FWHM, as shown in Figure 9(b), can clearly show the change of the structure of the ice at various temperatures. In the temperature range 117 ~ 163 K, the FWHM maintains at 4.5 times the reference value above 117 K, which indicates that the distribution pattern of oxygen atoms' spacing is almost unchanged, implying the competition mechanism between the melting-induced weakening and pulverisation-induced strengthening as the temperature decreases.

The tensile fracture behaviour of the ice at 100 and 73 K is shown in Figure 10. It can be seen that with decreasing the temperature from 100 to 73 K, the fibrous fracture morphology disappears, and the fracture surface is getting more flat with the significant decrease of the fracture surface area from 29.48 to 19.21 nm^2, indicating the ductile-to-brittle fracture transition of the ice accounting for the decrease of the dynamic tensile strength at 73 K as depicted in Figure 5.

4. Conclusions

In this paper, the temperature-dependent dynamic tensile strength of the ice described by the SPC/E force field is studied by MD simulations. The main conclusions are as follows.

(1) The dynamic tensile strength of the ice shows an anomalous temperature effect with decreasing the temperature from 215 to 73 K. In the temperature range 117 ∼ 163 K, the dynamic tensile strength of the ice is insensitive to the temperature.

(2) The solid–solid transformation and the pentagonal-heptagonal defects are observed under dynamic compression, leading to the spalling of the damage region with the defects under subsequent dynamic tensile loading at temperatures above 163 K.

(3) The temperature insensitivity of the dynamic tensile strength of the ice in the temperature range 100 ∼ 163 K results from the competition mechanism between melting-induced weakening and pulverisation-induced strengthening.

(4) The ductile-to-brittle failure mode occurs with decreasing the temperature from 100 to 73 K, leading to a decrease of the dynamic tensile strength of the ice.

Acknowledgments

Disclosure statement

No potential conflict of interest was reported by the author(s).

Funding

References

[1] R.A. Bindschadler, *Tidally controlled stick-slip discharge of a west antarctic ice*. Science. 301 (2003), pp. 1087–1089.

[2] P. Voosen, *New feedbacks speed up the demise of Arctic sea ice*. Science. 369 (2020), pp. 1043–1044.

[3] L.M. Prockter, *Ice in the Solar System*. Johns Hopkins APL Tech. Dig. 26 (2005), pp. 175–188.

[4] J.J. Petrovic, *Review Mechanical properties of ice and snow*. J. Mater. Sci. 38 (2003), pp. 1–6.

[5] J.H. Currier and E.M. Schulson, *The tensile strength of ice as a function of grain size*. Acta Metall. 30 (1982), pp. 1511–1514.

[6]   E. Schulson, *The brittle compressive fracture of ice*. Acta Metall. Mater. 38 (1990), pp. 1963–1976.

[7]   E.M. Schulson, D. Iliescu and C.E. Renshaw, *On the initiation of shear faults during brittle compressive failure: a new mechanism*. J. Geophys. Res. 104 (1999), pp. 695–705.

[8]   M. Arakawa and N. Maeno, *Mechanical strength of polycrystalline ice under uniaxial compression*. Cold Reg. Sci. Tech. 26 (1997), pp. 215–229.

[9]   X. Wu and V. Prakash, *Dynamic compressive behavior of ice at cryogenic temperatures*. Cold Reg. Sci. Tech. 118 (2015), pp. 1–13.

[10] Q. Yin, L. Hu, X. Wu, K. Xiao and C. Huang, *Temperature-dependent phase transformation of ice-1 h under ultrafast uniaxial compression: a molecular dynamics simulation*. Comput. Mater. Sci. 162 (2019), pp. 340–348.

[11] H.J.C. Berendsen, J.R. Grigera and T.P. Straatsma, *The missing term in effective pair potentials*. J. Phys. Chem. 91 (1987), pp. 6269–6271.

[12] Z. Zhang and Z. Duan, *Prediction of the PVT properties of water over wide range of temperatures and pressures from molecular dynamics simulation*. Phys. Earth Planet. Inter. 149 (2005), pp. 335–354.

[13] T. Bryk and A.D.J. Haymet, *Ice 1 h/water interface of the SPC/E model: molecular dynamics simulations of the equilibrium basal and prism interfaces*. J. Chem. Phys. 117 (2002), pp. 10258–10268.

[14] S.C. Gay, E.J. Smith and A.D.J. Haymet, *Dynamics of melting and stability of ice 1h: molecular-dynamics simulations of the SPC/E model of water*. J. Chem. Phys. 116 (2002), pp. 8876–8880.

[15] E.M. Schulson and P. Duval, *Creep and fracture of ice*, Cambridge University Press, Cambridge, 2009.

[16] S. Plimpton, *Fast parallel algorithms for short-range molecular dynamics*. J. Comput. Phys. 117 (1995), pp. 1–19.

[17] J. Delhommelle and P. Millié, *Inadequacy of the Lorentz-Berthelot combining rules for accurate predictions of equilibrium properties by molecular simulation*. Mol. Phys. 99 (2001), pp. 619–625.

[18] W.G. Hoover, *Canonical dynamics: equilibrium phase-space distributions*. Phys. Rev. A. 31 (1985), pp. 1695–1697.

[19] A. Stukowski, *Computational analysis methods in atomistic modeling of crystals*. J Miner Met Mater Soc 66 (2014), pp. 399–407.

[20] A. Stukowski, *Visualization and analysis of atomistic simulation data with OVITO–the open visualization tool, modelling simul*. Mater. Sci. Eng. 18 (2010), p. 015012). https://iopscience.iop.org/issue/0965-0393/18/1.